nature chemical engineering

Article

https://doi.org/10.1038/s44286-023-00023-z

Reconfigurable liquid devices from liquid building blocks

Received: 30 May 2023

Accepted: 17 December 2023

Published online: 5 February 2024

Check for updates

Yi Zeng[1,2], Sen Li[1,2], Zhejun Chong[1,2], Yanfang Niu[1], Keliang Liu[1], Jiankang Zhou[1], Zhenzhu He[1], Junning Zhang[1], Jing Zhao[1], Shuang Ding[1], Xin Du[1] ✉ & Zhongze Gu[1] ✉

Liquids are widely applied in the construction of various functional devices due to their abilities to flow, dissolve, deform and phase separate; however, the fabrication of liquid-based devices can be costly and lack reconfigurability due to the need for predesigned solid enclosing walls. Herein we report a strategy to generate and manipulate functional liquid devices by assembling and disassembling different types of liquid droplets like toy building blocks; we also uncover the underlying mechanisms. Multiphase liquid devices with diverse compositions and geometries can be quickly constructed and reconfigured in a pillared substrate, enabling the ability to freely structure liquids and precisely program liquid–liquid interfaces. The applications in fluidic devices, microreactors and their combinations are demonstrated.

A wide range of distinct liquids—including hydrophilic liquids, hydrophobic liquids, perfluorinated amphiphobic liquids, ionic liquids[1], coacervates[2–4], ferromagnetic liquids[5] and liquid metals[6,7]—form a large library that fulfills the demands of different scientific and societal applications. When blended, miscible liquids combine to form homogeneous solutions, whereas immiscible liquids quickly generate asymmetric liquid–liquid interfaces that can stabilize, structure and transport specific matter[8–11]. These unique features make liquids ideal materials for building complex devices for diverse applications. During the past decades, many efforts have been devoted to the generation of functional devices based on static or flowing liquid parts, and these devices have shown great potential as advanced platforms in, for example, synthesis, bio-incubation, diagnosis and micro/nanofabrication[5,12–16].

Normally, a liquid-based device requires pre-fabricated solid walls to confine the flowable liquid to a pre-designed area, which considerably raises the time and cost required for the device fabrication. It also greatly increases the difficulty of device reconfiguration, induced by instantaneous decisions made when performing optimizations or solving unexpected situations[17]. Substantial progress has been made in developing wall-free strategies to manipulate liquid droplets and flows, specifically molding their shapes and steering directional movements[18–21] by utilizing textured structures[22,23], superwettable patterns[24,25], stimulus-driven substrates[26] and nanoparticle-reinforced water–oil interfaces[27], among others[28–31]. However, constructing multiphase liquid devices, precisely aligning liquid–liquid interfaces and reconfiguring liquid structures on-demand are still obstacles faced by these systems.

Inspired by modular construction toys, where complex and reconfigurable models could be assembled through interlocking and dismantling building blocks, we considered that liquid devices might be constructed by the direct assembly of liquid units. Herein we proposed an approach to construct liquid devices with reconfigurable complex geometries and precisely arranged liquid–liquid interfaces (Fig. 1a). Leveraging a pillared substrate incubated in silicone oil (Fig. 1b), the liquid units are in situ produced owing to their surface tension. The adjacent miscible liquid units spontaneously connect with each other leading to homogenous liquid structures, whereas the immiscible liquid units build desired liquid–liquid interfaces at specific positions. In that manner, 2D and 3D liquid devices with diverse geometries, compositions and well-designed liquid–liquid interface arrangements could be constructed in minutes. Moreover, the liquid building blocks strategy allows the user to dismantle and remove liquid units on demand and reconfigure the design and function of the as-fabricated liquid structures. We discuss the mechanisms underlying this strategy and

[1]State Key Laboratory of Digital Medical Engineering, School of Biological Science and Medical Engineering, Southeast University, Nanjing, China. [2]These authors contributed equally: Yi Zeng, Sen Li, Zhejun Chong. ✉e-mail: du.xin@seu.edu.cn; gu@seu.edu.cn

https://doi.org/10.1038/s44286-023-00023-z

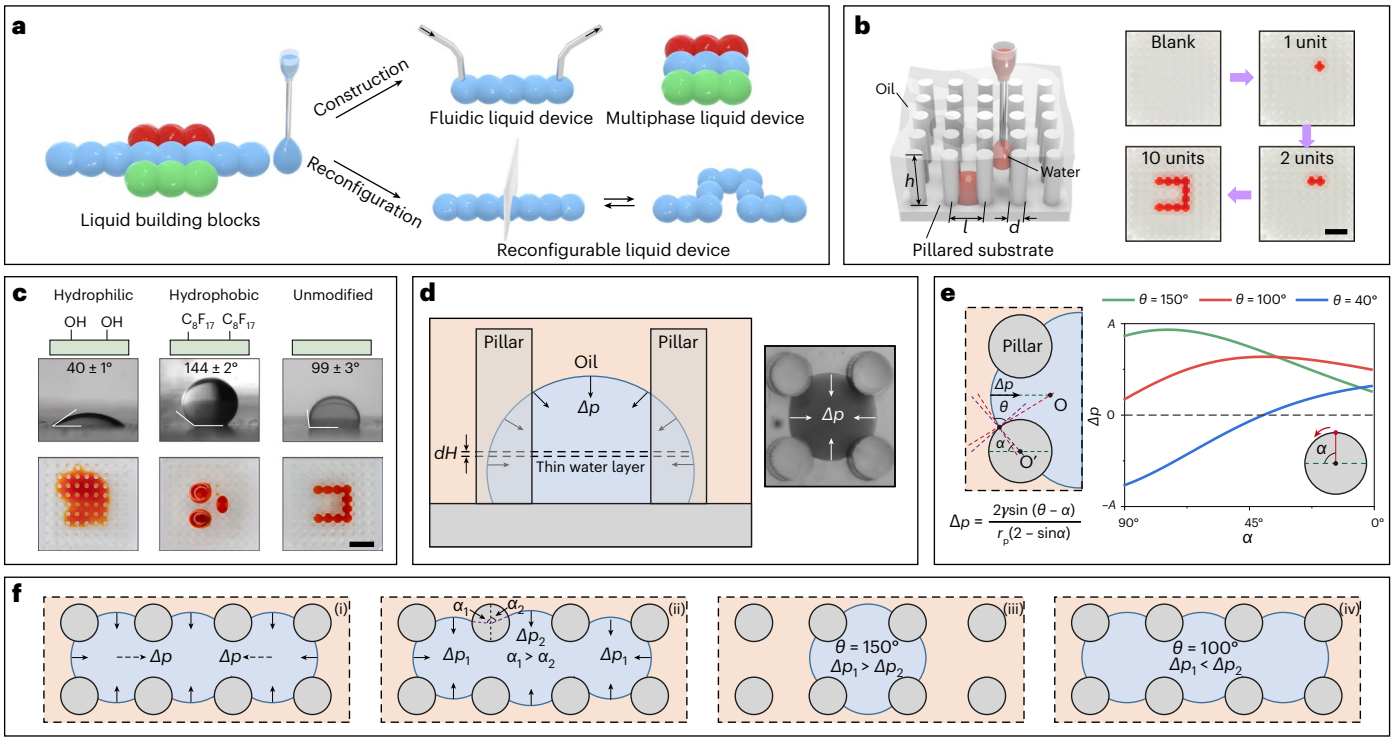

Fig. 1 | Demonstration of the liquid building blocks concept. a, Schematic representation of the liquid building blocks strategy, enabling the construction and reconfiguration of liquid devices. **b**, Left: design of the pillared substrate for liquid building blocks. Right: formations of water unit and aqueous structures in the pillared substrate (h = 5 mm, l = 2 mm, d = 1 mm). **c**, Investigations into the formations of aqueous channels in pillared substrates with different hydrophobicities. **d**, Mechanistic analysis of a thin water layer (dH) in a water unit in the pillared substrate. Left: cross-sectional view. Right: top view. The Δp term refers to the Laplace pressure of the curved water–oil interface. **e**, Change of LP when the water–oil interface expands (α decreases) in different types of pillared substrates; $A = \frac{2\gamma}{r_p}$. See Supplementary Note 1 and Supplementary Fig. 2 for more details. **f**, Illustrated demonstration of LP changes in three connected water units in the pillared substrate. Four stages are shown: (i) the initial state; (ii) transition state; (iii) final stage in the pillared substrate with θ = 150°; (iv) and final stage in the pillared substrate with θ = 100°. Scale bars, 5 mm.

demonstrate its potential applications in fluidic devices, microreactors and their combinations.

Results

Generation of liquid units and their assemblies

The first step in realizing liquid building blocks is to create and fix liquid units. In our work, using the Laplace pressure (LP) of a curved liquid surface, we designed and printed a pillared substrate using a commercial 3D printer with acrylate epoxy resin to trap the liquid units (Fig. 1b and Supplementary Fig. 1a). When a 10 µl water droplet (Supplementary Fig. 2a) was added to the pillared substrate incubated in silicone oil, the water droplet was trapped by the surrounding four pillars to form a stable water unit (Supplementary Video 1). By continuously adding water droplets into the pillared substrate, more water units were formed and eventually connected into a structured water channel (Fig. 1b and Supplementary Video 1). Interestingly, as we found when using 10 µl water for each unit, the formation of a water channel was highly dependent on the surface energy of the substrate material. As shown in Fig. 1c, the bare resin of the pillared substrate exhibited a water contact angle (WCA, measured in silicone oil) of 99 ± 3°, the oxygen-plasma-treated resin led to a hydrophilic surface (WCA = 40 ± 1°), and the fluorinated resin exhibited high hydrophobicity (WCA = 144 ± 2°). The hydrophilic pillared substrate could not trap the water droplets, which quickly spread between the pillars (Fig. 1c, left). The fluorinated pillared substrate could trap the water units, but the connected water units automatically contracted to break the as-formed channel (Fig. 1c, middle). The bare pillared substrate with a medium hydrophobicity could stabilize the formed water channel (Fig. 1c, right).

It is challenging to fully understand this phenomenon as a water droplet in the pillared substrate bears forces in the upward, lateral and downward directions, which induces a complex model for mechanistic analysis. A simplified model was established when considering a thin layer of the water unit (Fig. 1d). The water layer has the tendency to spread between the pillars due to its interaction with the pillar walls; however, such a process is resisted by the LP (Δp) induced from the convex water–oil interface, making the water layer mechanically stable. The Δp term can be calculated using the following equation (see Supplementary Note 1 and Supplementary Fig. 2 for a detailed derivation of equation (1))[32]:

$$\Delta p = \frac{2\gamma \sin(\theta - \alpha)}{r_p(2 - \sin\alpha)} \quad (1)$$

where r_p is the radius of the pillar, γ is the surface tension of water, θ is the WCA of the substrate material, and α is an angle indicating the position of the water–oil interface in the pillar array. As the water volume in a unit increases, the water–oil interface continuously moves towards the oil side (α decreases) and Δp changes accordingly. The relationships between calculated Δp and α in pillared substrates with different surface energies are shown in Fig. 1e. For the hydrophilic pillared substrate ($\theta = 40^o$), Δp is negative when α is larger than 40°, meaning that the LP helps the expansion of the water–oil interface. As the water–oil interface further expands and α decreases, Δp tends to be positive but is rather small and may not be able to restrict the water droplet; thus, the water unit quickly spreads between the pillars, matching the experimental result (Fig. 1c, left). When the pillared substrate

is more hydrophobic ($\theta = 150°$ and 100°), Δp remains positive and therefore stable water units can be obtained in these cases (Fig. 1c, middle and right).

We simulated a thin water layer in a water channel (three connected water units) to explore the phenomena during the generation of multiple-unit liquid structures. Compared with a single water unit, the water units at both ends of the channel bear additional pressures directed to the central unit, owing to the combination (loss) of some water–oil interfaces (Fig. 1fi). As a result, the water units at both ends tend to flow to the central unit, causing α to decrease and increase in the central and end units, respectively (Fig. 1fii). In the highly hydrophobic pillared substrate ($\theta = 150°$), the Δp of the water–oil interfaces increases along with increase of α. As a consequence, the LP in the central unit (Δp_2) would be smaller than that of the end units (Δp_1) when water moves from end units to the central unit, triggering the contraction of the connected units to break the as-formed channel (Fig. 1fiii). By contrast, in the slightly hydrophobic pillared substrate ($\theta = 100°$), Δp decreases when α increases from 40° to 90°; thus, Δp_2 would be larger than Δp_1, preventing the further contraction of the connected units and therefore stabilizing the water channel (Fig. 1fiv). These results are also confirmed by a numerical simulation of a 2D water layer (Extended Data Fig. 1), and computational fluid dynamics (CFD) simulations of the combination of two water units (Extended Data Fig. 2 and Supplementary Video 2). Note that this simplified model is based on the premise that the water–oil interface is spherical. Once the volume of the water unit further increases, the water–oil interface will gradually become ellipsoidal or even cylindrical (Supplementary Fig. 3), potentially limiting the applicability of this simplified model (as discussed in Supplementary Note 1).

Pillars with different shapes (triangle, diamond, square, pentagon and hexagon) were also investigated (Extended Data Fig. 3). We found that only diamond pillars exhibited a similar performance to circular pillars. For pillars with other shapes, contraction occurred frequently when adding water droplets or connecting water units. The phenomenon could be understood by calculating the change in Δp of a thin water layer during the expansion of the water–oil interface between pillars (Extended Data Fig. 4). For square and hexagon pillars, there are break points of the Δp value when the water–oil interface expands (α decreases), making such an expansion process inhomogeneous and thus uncontrollable. For diamond pillars, there is no break point of LP when α decreases from 90° to 0°, which minimizes the possible contraction during liquid channel formation. Therefore, in this system, the surface energy of substrate material, liquid volume and the geometry of pillared substrate collectively determine the generation of liquid units and their assemblies, which could be explored further. Notably, in our system, to form stable water units, the density of the oil should be lower than that of water (Supplementary Fig. 4a). For example, when the silicone oil was replaced with FC40, a fluorinated oil with a density of 1.8 g cm^{-3}, water units were not stable and flowed to the top of the oil in our system (Supplementary Fig. 4b).

Fluidic liquid devices

With the help of a push–pull syringe pump (see Methods), the connected liquid units in the pillared substrate could work as a fluidic channel, as confirmed by the color exchange when pumping dye solutions through the channel (Fig. 2a). The flow field in the channel was visualized using tracer particles (Supplementary Video 3), verifying the unidirectional flow of liquid in the channel. To demonstrate the significance of the curved water–oil interfaces between pillars, we tested the maximum flow rates that straight (~20 mm in length) and curved (~30 mm in length) channels could withstand (Supplementary Fig. 5). The results indicated that the maximum flow rate in such channels was at least 200 ml h^{-1}, which is greater than that of previously reported all-liquid fluidic configurations (based on hydrophilic–hydrophobic patterns, 10 ml h^{-1} for a 2-mm-wide channel)[27]. When pumping starts without pillar arrays, the water droplets at the inlet and outlet of the hydrophilic–hydrophobic pattern would expand and shrink, respectively (Fig. 2b, top). In this scenario, the LP at the inlet (Δp_1) would be lower than the LP at the outlet (Δp_2), impeding the flow of water from inlet to outlet, leading to leakage of the solution and therefore damaging the channel design (Supplementary Fig. 6). Conversely, by leveraging the pillared substrate, the change of LP follows equation (1) when the water–oil interface expands, leading to a higher LP at the inlet and a lower LP at the outlet. That way, the fluidic channel in the pillared substrate obtains enhanced stability at high pumping rates (Fig. 2b, bottom; see Supplementary Fig. 7 and Supplementary Note 2 for a more detailed analysis). As characterized in 1 h pumping studies, the fluidic channels in the pillared substrate remained stable at flow rates of 10 ml h^{-1} and 40 ml h^{-1} (Supplementary Fig. 8a).

Taking advantage of the liquid building blocks strategy, fluidic structures (Fig. 2c) with relatively simple designs could be constructed via a flexible manual process (Supplementary Videos 1 and 4), whereas fluidic structures with complex geometries could be created automatically in minutes using a customized dispensing machine (Fig. 2d and Supplementary Videos 5 and 6). All of these diversified fluidic structures were constructed in the same designed pillared substrates, rendering the continuous directional transport of fluid in different geometries; however, for fluidic devices based on solid walls or superwetting-textured structures, the path of liquid directional transport is predefined, restricting the versatility of the substrate for different applications. Fluidic channels at diverse scales could also be generated when the size of the pillared substrate was proportionally magnified or reduced (Supplementary Fig. 9a). The values of Δp and α under various pillar radii (r_p = 200, 300, 400, 500, 800, 900 and 1,000 μm), were calculated (Supplementary Fig. 9b). The relationships between Δp and α in these curves were quite similar, explaining the feasibility of fluidic channel formation under different pillar radii.

The effect of gravity is minimized in this system as the generated liquid structure was quite stable even if the pillared substrate was tilted 90° (Supplementary Fig. 10). Water evaporation, as well as liquid channel stability and molecular absorption in the fabricated liquid devices, were also investigated (Supplementary Figs. 11–14). After 24 h, ~84% water of the liquid unit was maintained, indicating minor water evaporation of our design (Supplementary Fig. 11). The WCA of the pillared substrate material remained at ~100°, and the liquid channel structure was quite stable except minor water evaporation after a six-day assessment (Supplementary Fig. 12). For the molecular absorption tests, the liquid devices showed negligible absorption for hydrophilic bovine serum albumin (BSA) molecules (Supplementary Fig. 13), whereas substantial hydrophobic molecular absorption (Rhodamine B) was detected after 2 h static observation compared with commercial PDMS chips (Supplementary Fig. 14), which was attributed to the absorption of hydrophobic molecules by oil.

Multiphase liquid devices

Other types of liquids besides water can be applied to create liquid units with this strategy (Fig. 3a). Liquids with various surface tensions were added into the pillared substrate, and their performances were found to be highly related to the contact angle of the liquid on the substrate material (Fig. 3b and Supplementary Fig. 15). The effects of surface tension and contact angle on the generation of liquid unit were investigated. The geometry of the liquid unit was determined by the contact angle, and the expansion speed of the liquid–oil interface was dominated by the surface tension (Supplementary Fig. 16). Therefore, the generation of a stable liquid unit is typically dependent on an appropriate contact angle of liquid. According to this, different types of liquids could be adopted to greatly enhance the versatility of our strategy. For example, the adoption of hydrogel precursors could generate hydrogel units that are potentially important for biological

https://doi.org/10.1038/s44286-023-00023-z

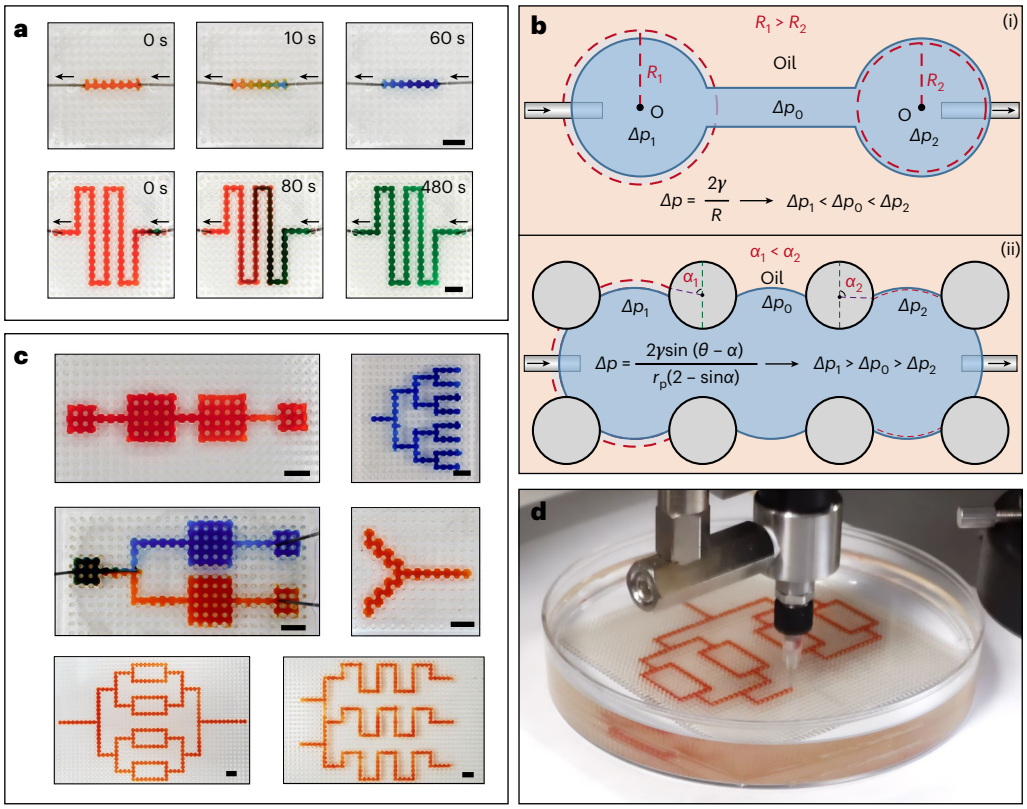

Fig. 2 | Fluidic liquid devices. a, Pumping solution with dye into straight and curved fluidic channels in the pillared substrate led to color change, showing the substitution of the liquids in the channels. **b**, Changes of water–oil interface and LP of a thin liquid layer at the inlet and outlet of a fluidic channel (i) without and (ii) with pillar arrays. The red dash refers to the water–oil interface when pumping starts. *R*, the radius of curvature of the water–oil interface. **c**, Fluidic devices with various geometries could be formed in the pillared substrate. **d**, Complex liquid structures can be automatically fabricated with customized equipment. Scale bars, 5 mm.

applications (Supplementary Fig. 17a); liquid metal (LM) could be introduced to endow the device with conductivity (Supplementary Fig. 17b); and an omniphobic liquid, Krytox[33], could be utilized as a functional liquid to generate liquid walls that prevent the diffusion of liquids with small contact angles, which would permit the use of many organic solvents (Fig. 3bi). When the adjacent liquid units were immiscible, a liquid–liquid interface automatically formed at their boundary (Fig. 3bii, Supplementary Fig. 18), allowing the selective extraction or transportation of specific matters. Liquid devices with multiple well-arranged liquid–liquid interfaces could be quickly assembled by leveraging the liquid toolbox, which is difficult to achieve with other construction methods due to their limitations in the available liquid types.

An example of a multiphase liquid battery is shown in Fig. 3c, where one was fabricated using an aqueous unit (containing 0.1 M hydroquinone and 0.1 M HCl), an ionic liquid (IL) unit (0.1 M parabenzoquinone dissolved in 1-butyl-1-methylpyrrolidinium bis(trifluoromethylsulfonyl)imide ($PyR_{14}TFSI$)), two LM units, and some Krytox units as liquid walls to prevent the diffusion of IL (Fig. 3ci). As water, IL and LM are immiscible, water–IL, water–LM and IL–LM interfaces were generated in this device. The aqueous unit served as the catholyte, whereas the IL unit served as the anolyte; there is not any physical separator or ion-exchange membrane because the water–IL interface prevents the blending of redox reagents but allows the transportation of protons. The two LM units worked as electrodes, considering that the water–LM and IL–LM interfaces allowed electrons to cross freely. In this scenario, the all-liquid device worked as a rechargeable membrane-free mini battery[34], as confirmed by the charge–discharge test and open-circuit voltage measurement (0.21 V for a one-unit battery). Owing to the flexibility of our strategy, all-liquid batteries with various geometric designs (Fig. 3cii) or different electrolyte compositions (Supplementary Fig. 19a) could be easily constructed to regulate and optimize the electronic performances. As shown in Fig. 3ciii and Supplementary Fig. 19b, series-connected liquid batteries (one to five repeating units) were generated, and their output voltages showed a linear increase. Compared with other membrane-free battery designs, our strategy enabled the fast construction of multicomponent battery within minutes, and the convenient optimization of battery performance through in situ engineering liquid unit assembly patterns.

Such multiphase liquid devices could also be demonstrated as microreactors for cascade chemical reactions. The multiple interfaces of liquid building blocks work as compartments for the incompatible reagents, making one-pot syntheses possible. As shown in Fig. 3d, a multiphase liquid device was constructed so that anisyl alcohol could be synthesized from *p*-(dimethoxymethyl) anisole in one pot using HCl and $NaBH_4$. The incompatible HCl and $NaBH_4$ units were separated by an immiscible IL unit, while the *p*-(dimethoxymethyl) anisole in the IL unit could react with HCl and $NaBH_4$ at their respective water–IL interfaces to perform the cascade reaction. We tested the stability of the multiphase device, finding that it was stable over 24 h, and no obvious communication between two aqueous units was observed (Supplementary Fig. 20). The cascade reaction was then performed using this device. As analyzed by gas chromatography, the product anisyl alcohol was synthesized, and showed the highest mass fraction at 72% after 24 h under 0.75 mol l^{-1} $NaBH_4$ in our system. With the liquid building blocks strategy, the complex processes associated with the stabilization of multiple liquid–liquid interfaces using Pickering

https://doi.org/10.1038/s44286-023-00023-z

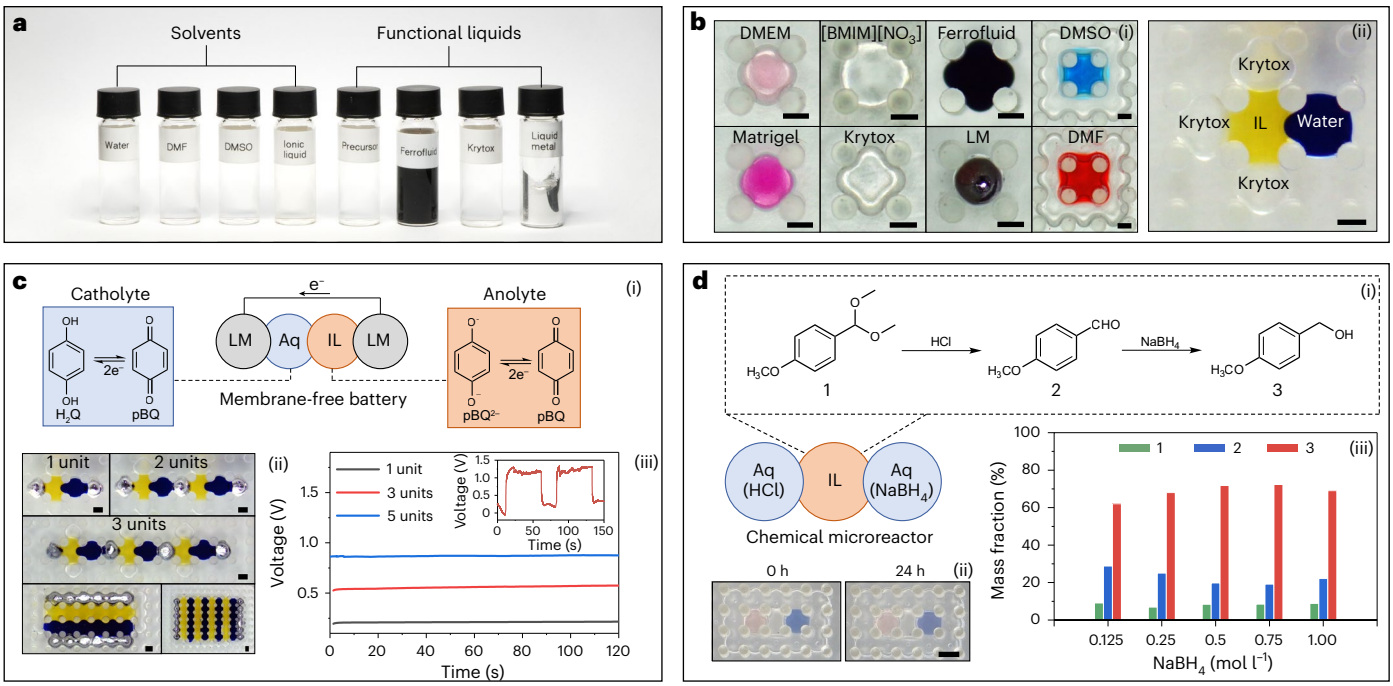

Fig. 3 | Multiphase liquid devices. a, Examples of the available liquids involved in the liquid building blocks strategy. **b**, Behaviors of diverse liquids in the pillared substrate. (i) Photographs of the liquid units generated with different liquids; the DMSO and DMF units are surrounded with Krytox walls to prevent their diffusion. (ii) Liquid–liquid interfaces generated with immiscible units (water, Krytox and $PyR_{14}TFSI$). Scale bars, 1 mm. DMEM, Dulbecco's Modified Eagle Medium; [BMIM][NO_3], 1-butyl-3-methylimidazolium nitrate. **c**, A membrane-free battery generated with an aqueous unit, an IL unit and two liquid metal units. (i) The structure and mechanism of the battery; (ii) photographs of the batteries with different structural designs (4 mg ml^{-1} methylene blue was added into the aqueous units to make them visible); (iii) open-circuit voltage of the batteries with one, three and five repeating units (the inset is the charge–discharge curve of the one-unit battery). Scale bars, 1 mm. H_2Q, hydroquinone; pBQ, parabenzoquinone. **d**, One-pot synthesis of anisyl alcohol using liquid-building-blocks-constructed multiphase microreactors. (i) The design of the microreactor and the mechanism of the one-pot synthesis; (ii) liquid–liquid interface stability test; (iii) and the contents of the one-pot synthesis under different $NaBH_4$ concentrations. Scale bar, 2 mm.

emulsions or lipid membranes are bypassed, and the positions of the different phases as well as their interfaces could be precisely controlled. This shows the capability of our strategy in building complex microreactors for multistep synthesis.

Aside from the 2D liquid devices above, our liquid building blocks approach can also build liquid structures with 3D configurations by modifying trays on the pillar (Supplementary Figs. 1b and 21a). Water units can be held by the four trays with the help of the bottom water–oil interfaces (Supplementary Fig. 21b), enabling the formation of suspended structures and multi-layer structures. Thus, fluidic devices with 3D branched channels (Supplementary Fig. 21c) and intertwined-but-independent 3D channels (Supplementary Fig. 21d), and 3D multiphase liquid devices (Supplementary Fig. 21e), could be generated in this manner, which was challenging for previously reported methods. The generated 3D liquid structures were also stable over time (Supplementary Fig. 22) and could afford fluid pumping to some extent (Supplementary Figs. 8b and 23). The flow field tests indicated the unidirectional flow of liquid from inlet to outlet despite the height of the fluidic channels (1–4 layers, Supplementary Video 7 and Supplementary Fig. 24).

Reconfigurable liquid devices

The demand for liquid devices has evolved from simply driving liquid through predefined paths, to switching device configurations, dealing with the real-time decisions and needs of multiple functionalities integrated on one device. State-of-the-art reconfigurable liquid devices generally harness numerous valves in predesigned channels, stimulus-responsive hydrogels, and electrowetting technology[17]. However, the substantial issues with current methods—regarding expensive equipment, complex operation and liquid residue contamination—restrict the popularity and development of reconfigurable liquid devices. Inspired by the reconfiguration feature of toy building blocks, the liquid devices constructed using our strategy enable the desired reconfigurations without the concerns of cost, time and experience through the fast connection, cutting and removal of liquid units. The as-formed water channel could be quickly disconnected by cutting it with a fluorinated paper sheet (Fig. 4a and Supplementary Fig. 25); the disconnected water units could then be removed using a pipette (Supplementary Video 8). During the cutting process, we found that the tri-phase contact line of the water channel receded (Extended Data Fig. 5). The possible mechanism was illustrated in Fig. 4b (see Extended Data Fig. 5 and Supplementary Note 3 for more details). When the fluorinated paper is inserted into a water unit, the water–oil interface in the unit bears forces that drive the interface up and down, respectively. The water unit could be cut off only when the downward forces beared by the water–oil interface during reconfiguration (F_{down}) is larger than F_{up}; that is, equation (2) should be satisfied.

$$\frac{\cos\beta}{\cos\theta} > \frac{4}{2\sqrt{2}-1} \tag{2}$$

where θ is the WCA of the pillared substrate and β is the WCA of the fluorinated paper sheet. In our research condition, $\theta \approx 100°$, $\beta \approx 160°$ and $\frac{\cos\beta}{\cos\theta} \approx 5.41 > \frac{4}{2\sqrt{2}-1}$, and thus the water unit can be easily cut off. By contrast, in fluorinated pillared substrates (Supplementary Fig. 26), $\frac{\cos\beta}{\cos\theta} \approx 1.16 < \frac{4}{2\sqrt{2}-1}$, and thus the channel cannot be cut off.

The reconfigurable characteristic of liquid building blocks enables the connection, cutting and alternation of liquid structures in minutes,

https://doi.org/10.1038/s44286-023-00023-z

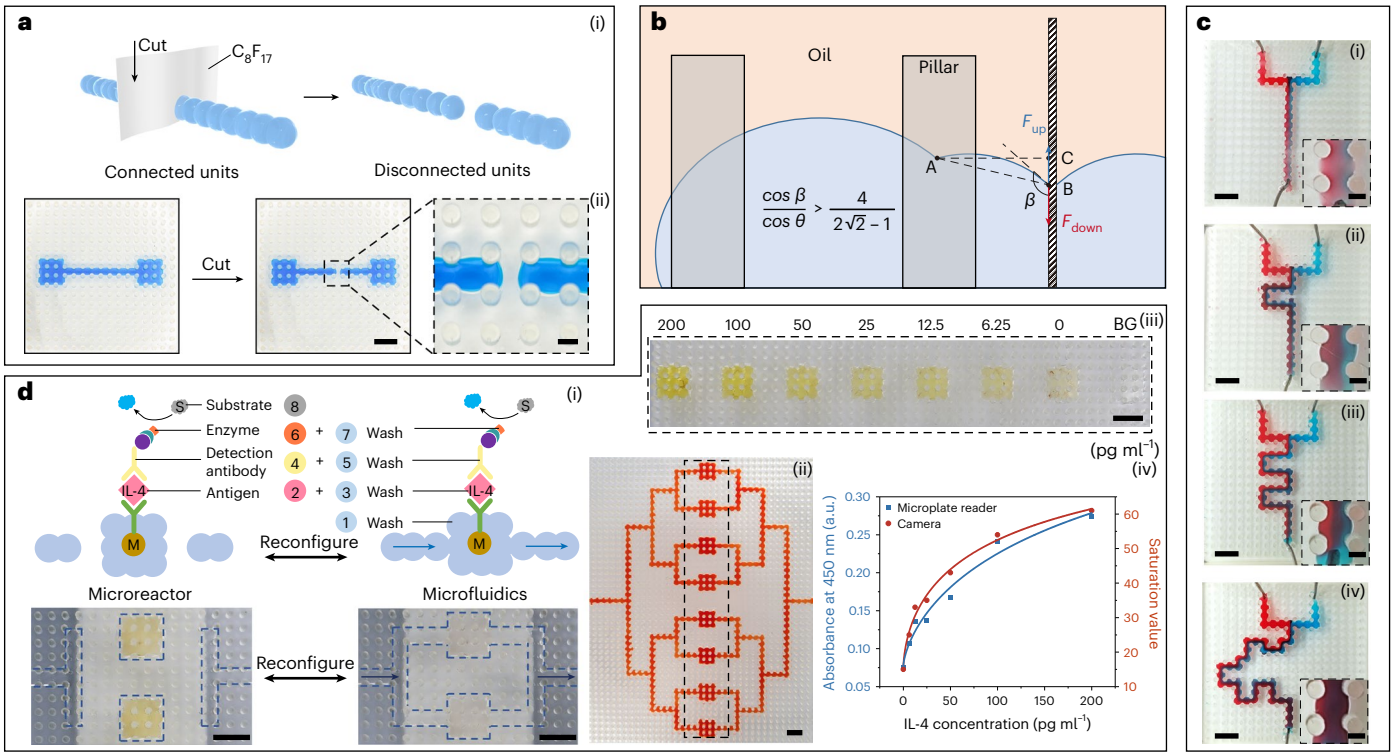

Fig. 4 | Reconfigurable liquid devices. a, Connected liquid units could be cut off with a fluorinated paper sheet. (i) Schematic illustration of the cutting process; (ii) photos of an aqueous channel before and after being cut off with a fluorinated paper sheet. Scale bars, 5 mm (1 mm in the magnified image). **b**, Mechanistic analysis of the disconnection process (see Extended Data Fig. 5 and Supplementary Note 3 for details). **c**, The architectures of the fluidic channels were reconfigured on demand, regulating the blend of the liquids in the device. Scale bars, 5 mm (1 mm in the magnified images). **d**, Human IL-4 protein ELISA performed in a reconfigurable liquid device. (i) The eight steps in common ELISA protocols were sequentially performed through the reconfiguration of the liquid device; (ii) a photo of the reconfigurable liquid device; (iii) the assay results captured by a camera; (iv) the binding curves obtained by analyzing the final solutions with a microplate reader and extracting color saturation values from the image in (iii). BG, background. Scale bars, 5 mm.

which is challenging for current liquid devices (Fig. 4c and Supplementary Video 9). We considered that such features might make it possible to integrate multiple laborious experimental steps—such as alternating reactions and washes—into one device. Enzyme-linked immunosorbent assay (ELISA), possessing the enzymatic amplification effect, is a mainstream biomedical analysis method in laboratories; however, ELISA is a labor-intensive assay regarding multiple incubations and dozens of wash steps. We therefore proposed performing ELISA on our liquid-building-blocks-built device in an efficient, economical and convenient way for potential point-of-care assays.

As demonstrated in Fig. 4d, the eight steps of human IL-4 protein ELISA (Fig. 4di) were performed on a liquid-building-blocks-constructed chip with the illustrated fluidic channels (Fig. 4dii). When the fluidic channels were cut off, microreactors formed to support the reactions of steps 2, 4, 6 and 8, avoiding the waste of expensive reagents remaining in the flow channels, syringe pumps and their connecting parts. When the microreactors were connected with the surrounding fluidic channels, laborious washing steps 1, 3, 5 and 7 were performed by the push–pull syringe pump connected to the inlet/outlet of the main channel, allowing for a spontaneous wash. 3,3′,5,5′-Tetramethylbenzidine was used as the substrate so that the colorimetric results could be distinguished by the naked eye/cameras, or a commonly used microplate reader. As shown in Fig. 4diii,iv, human IL-4 protein could be quantified in the 6.25 pg ml^{-1} to 200 pg ml^{-1} range, which is consistent with the detection range in the common 96-well-plate-based protocol provided by the manufacturer. Notably, the constructed chip is an open device, allowing sampling anytime in any area of the chip without disturbance of air bubbles, which is unattainable in common fluidic-chip-based assays.

Discussion

In summary, inspired by toy building blocks, we proposed the liquid building blocks strategy for the fast construction and in situ reconfiguration of liquid devices. We showed that complex and stable liquid devices, including fluidic devices and multiphase devices, could be fabricated and reconfigured in minutes by directly assembling and disassembling the numerous liquid units; 2D and 3D liquid devices with diverse geometries, various liquid compositions and well-designed liquid–liquid interface arrangements were demonstrated. With this strategy, the manipulation and programming of liquids in a spatiotemporal way were realized, confirming sorts of promising applications including but not limited to fluidic chips and microreactors. Yet the proposed set-up also exhibits some limitations at the current stage. 3D fluidic channels require further substrate structure optimizations to enhance the operation stability, especially under high flow rates. The more complex chemical reactions, involving intense energy exchange with the surrounding environment, are waiting to be explored in our system. This liquid building blocks strategy shows us a new path to liquid manipulation, deserving more optimizations and deeper investigations.

Methods

Materials

Acrylamide, gelatin methacryloyl and 1*H*,1*H*,2*H*,2*H*-perfluorodecyltrimethoxysilane (FAS) were purchased from Sigma-Aldrich; liquid metal (gallium indium alloy) was purchased from Aladdin; Matrigel was purchased from Beyotime; Fe_3O_4 nanoparticles were obtained from Nanorainbow; Krytox GPL 103 was purchased from Chemours; and water-soluble food dyes were purchased from Jiupin. The remaining

chemicals and materials were purchased from Macklin. Deionized water with a resistivity of 18.2 MΩ cm was used for the preparation of all aqueous solutions.

Fabrication of the pillared substrate

The predesigned 3D model of the pillared substrate was exported as an STL file and then imported to the 3D printer (Nova3D). The pillared substrate was printed in a layer-by-layer manner (layer thickness = 30 μm) with a photoresist (acrylate epoxy resin, Nova 3D) using the guidance of the software on the printer (NovaMaker v.2.5.9, www.nova3d.cn). The 3D printing process finished automatically and then the printed pillared substrate was washed with ethanol or isopropanol for 5 min, and further cured under 10 mW cm^{-2} blue light (420 nm) for 3 min.

Surface functionalization of the pillared substrate

The pillared substrate was exposed to O_2 plasma for 3 min with a plasma cleaner (CPC-A, CIF) to increase its hydrophilicity. FAS was coated on the substrate surface via chemical vapor deposition to increase its hydrophobicity; specifically, the freshly prepared pillared substrate and 2 ml FAS in a Petri dish were placed in a vacuum desiccator for 6 h, where the pressure was adjusted to −0.1 MPa using a vacuum pump.

Formation of liquid structures in the pillared substrate

First, the pillared substrate was placed in a Petri dish and covered with silicone oil (10 mPa s). Then liquid droplets were added between the pillars incubated in silicone oil with a pipette to form liquid units. The volume of the droplet depends on the size of the pillared array; 10 μl liquid was used as a droplet unit for the standard pillared array (h = 5 mm, l = 2 mm, d = 1 mm). Liquid structures were automatically formed by the spontaneous connection of adjacent liquid units (Supplementary Video 1). Liquid devices with different geometries can be fabricated following this method. Liquid channels could also be constructed using a syringe needle connected to a pump (flow rate = 10 ml h^{-1}) by slowly moving the needle in the pillared substrate (Supplementary Video 4). For automated fabrication, the pillared substrate was placed under a customized dispensing machine equipped with a triaxial displacement platform and a liquid dispensing valve (Supplementary Video 5). In that way, the liquid structures were automatically fabricated.

Pumping fluid through the fluidic channels

Syringe needles held by two probe heads were inserted into both ends of the fluidic channel and then connected to a push–pull syringe pump (LSP01-1C, Longer Precision Pump), as shown in Supplementary Fig. 27. Liquid could be pumped into the constructed fluidic channel under the pressure applied by the pump (Supplementary Video 6). Notably, when the viscosity of the liquid is high (for example, Krytox GPL 103, 82 cSt), the elastic deformation of the connecting tube and syringe in the pumping system will cause a substantial flow rate mismatch between the inflow and outflow, which may lead to overflow of the channel.

Numerical simulation of 2D water layer

The 2D simulation was performed using COMSOL Multiphysics (v.6.0, www.comsol.com). A model of three water units surrounded by oil in a pillar array was set up. The computational domain was set to 10 mm × 6 mm, and the total number of grids was set to 5,908. Both water and oil were assumed to be incompressible and Newtonian fluids, and the densities were assumed to be constant.

The flow within the liquids is governed by the Navier–Stokes equations, which can be expressed as:

$$\nabla \cdot \mathbf{U} = 0$$

$$\rho \frac{\partial \mathbf{U}}{\partial t} + \rho(\mathbf{U} \cdot \nabla)\mathbf{U} = \nabla \cdot [-p\mathbf{I} + \mu(\nabla \mathbf{U} + (\nabla \mathbf{U})^T)] + \mathbf{F}_{st}$$

where $\mathbf{U}$ represents the velocity, ρ represents the fluid density, μ represents the dynamic viscosity, T represents the temperature, p represents the pressure, and $\mathbf{F}_{st}$ represents the surface tension force. The initial condition of the velocity vector ($\mathbf{U}$) was set to 0.

Tracking the liquid–liquid interface plays a crucial role in this numerical simulation. As the liquid size is relatively small, the phase field method is a proper tool to reveal the flow mechanism. Instead of directly tracking the interface, the phase field method is governed by a phase field variable (ϕ). The whole computational domain is divided into the oil Ω_1 ($-1 \le \phi < 0$) and water Ω_2 ($0 < \phi \le 1$) subdomain, and the domain at $\phi = 0$ is the location of the water–oil interface (Extended Data Fig. 1a). As the phase field variable ϕ goes smoothly from −1 and 1, the computational region transforms from water to oil in terms of viscosity and density. The variable ϕ is governed by the Cahn–Hilliard equation, which can be written as:

$$\frac{\partial \phi}{\partial t} + \mathbf{U} \cdot \nabla \phi = \nabla \cdot \frac{\omega \lambda}{\varepsilon^2} \nabla[-\nabla \cdot \varepsilon^2 \nabla \phi + (\phi^2 - 1)\phi]$$

where ω represents the mobility (which determines the time scale of the Cahn–Hilliard diffusion), λ represents the mixing energy density and ε represents the thickness of the interface.

Furthermore, the wetted wall boundary condition was set for all pillar surfaces, and the remaining boundary was treated as a no-slip wall. The physical properties of the materials are listed in Supplementary Table 1.

Numerical simulations of 3D water droplets

The 3D droplet morphology simulation (Supplementary Figs. 4, 10 and 16) was conducted using the same method as the 2D water layer. A model containing a water unit trapped by four pillars in oil was established. The wetted wall boundary condition was applied to all substrates, and the remaining boundary was set as a no-slip wall. The impacts of gravity, density, surface tension and contact angle on the droplet morphology were investigated by altering the corresponding physical properties of the liquid (oil or water).

Computational fluid dynamics simulation of 3D water droplets

The water–oil interface was captured by the volume of fluid method[35] and the flow motion was solved by Navier–Stokes equation[36]:

$$\frac{\partial \alpha_d}{\partial \tau} + \nabla \cdot (\alpha_d \mathbf{U}) = 0$$

$$\frac{\partial \rho}{\partial \tau} + \nabla \cdot (\rho \mathbf{U}) = 0$$

$$\frac{\partial (\rho \mathbf{U})}{\partial \tau} + \nabla \cdot (\rho \mathbf{U}\mathbf{U}) = -\nabla p + \rho \mathbf{g} + \nabla \cdot \left[\mu \left(\nabla \mathbf{U} + \nabla \mathbf{U}^T\right)\right] + \mathbf{F}$$

where α_d is the volume fraction of water, and $\alpha_c = 1 - \alpha_d$ is the volume fraction of silicone oil, where $\mathbf{U}$, τ, p, $\mathbf{g}$ and $\mathbf{F}$ are the liquid velocity vector, flow time, liquid pressure, local acceleration vector of gravity, and source term of interfacial tension, respectively. The liquid density ρ and viscosity μ were calculated by the volume-fraction-averaged method[36]. The continuous surface force model presented by Brackbill et al.[37] was adopted to model the interfacial tension at the water–oil interface; this model converted the interfacial tension into a source term $\mathbf{F}$ for the momentum equation. Due to the difference in intermolecular forces among the silicone oil, water and pillared substrate, there was a contact angle θ between the water–oil interface and pillared substrate when they were in contact, which was considered in the simulations using the contact angle model[37].

The simulation was performed using the commercial CFD software ANSYS Fluent 18.0 (www.ansys.com). No-slip boundary conditions were used for the bottom wall and micro-pillar walls, and the top of computational field was set as the pressure outlet with an absolute pressure 1 atm. Periodic boundary conditions were implemented on the lateral faces of computational field. The volume of fluid equation was discretized by the explicit scheme, and the water–oil interface was reconstructed using a geometric reconstruction scheme based on the piecewise linear method. The Pressure-Implicit with Splitting of Operators algorithm was applied for the pressure–velocity coupling, and the second-order upwind scheme was employed for the spatial discretization of momentum equation. The discretization of transient terms was achieved by the first-order implicit scheme.

Molecular absorption tests

Hydrophilic BSA was chosen as a demonstration as BSA is commonly used in fluid-associated studies. A 20-mm-long fluidic channel was constructed, and 1 mg ml^{-1} BSA aqueous solution was pumped through the fluidic channel at 500 µl h^{-1}. After 2 h, the BSA concentration in the collected solution was tested with a microplate reader through Coomassie blue staining.

Hydrophobic Rhodamine B ($\log P = 2.4$) was also adopted to assess the molecular absorption of the liquid devices; 160 µl Rhodamine B solution (10 µg ml^{-1}) was added into a commercial PDMS channel (1.9 mm × 2.5 mm × 33.0 mm) and a 16-unit aqueous channel in a pillared substrate. Here the liquids in the PDMS and liquid-building-blocks-constructed chips had similar surface areas. The absorbance at 553 nm of Rhodamine B solution was measured with a microplate reader at different time points.

Formation of all-liquid membrane-free batteries

Batteries with different designs were generated in pillared substrates using a pipette. A biphasic liquid–liquid system was formed when aqueous catholyte (10 µl) and IL anolyte (10 µl) were added into the adjacent units (Krytox units were added before the addition of IL to prevent diffusion). Liquid metal (10 µl) was added at both ends of the catholyte and anolyte units to work as electrodes. Batteries with different designs were assembled in the same way. Electrochemical characterization of the battery was performed using an electrochemical workstation. To conduct chronopotentiometry cycling experiments, the battery was first discharged for 10 s at 1 µA to ensure a fully discharged state. The test was then performed at ±10 µA with a charging time of 50 s and a discharging time of 20 s. To measure the open-circuit voltage, the charged battery was put still for 5 min to ensure a stable state. The test time was set to 120 s.

Performing cascade chemical reactions in microreactor

A microreactor was generated with two aqueous units (one with 10 µl 0.01 mol l^{-1} HCl and another with 10 µl $NaBH_4$ at a specific concentration), an IL unit (containing 0.277 mol l^{-1} *p*-(dimethoxymethyl)anisole in $PyR_{14}TFSI$), and some Krytox units to prevent the diffusion of IL (the design of the device is shown in Supplementary Fig. 20). The device was incubated at 37 °C for 24 h. The solution was then pipetted from the IL unit and diluted 1,000 times with methanol for a gas chromatography test, with which we calculated the mass fraction of each compound to all compounds (raw compound 1, intermedium compound 2 and final product 3).

Construction of 3D fluidic channels

The 3D fluidic channels were fabricated manually using a pipette in a specifically designed pillared substrate (as shown in Supplementary Figs. 1b and 21a). The pipette tip was carefully inserted into the substrate. The position of the tip in the *z* direction can be visualized from the side. Liquid droplets (5–7 µl) were then slowly added between the pillars; a 3D fluidic channel could be fabricated by repeating the above process at different positions of the pillared substrate.

Reconfiguration of the connected water units

A fluorinated paper sheet was fabricated using filter paper (Whatman No. 1) and FAS using the chemical vapor deposition method described above. To disconnect a liquid structure, a fluorinated paper sheet was vertically inserted into the water unit and moved back and forth to 'cut' the unit. Highly hydrophobic materials such as Teflon film can also work in the same manner.

Enzyme-linked immunosorbent assay

An ELISA was performed using a commercial human IL-4 uncoated ELISA kit (Invitrogen, catalog no. 88-7046). The capture antibody was conjugated onto magnetic nanoparticles (MNPs) before performing the ELISA.

(1) Conjugation of IL-4 capture antibody onto MNPs
The MNPs used in the experiment are Dynabeads MyOne tosylactivated (Invitrogen), and the conjugation is performed following the protocol recommended by the producer. In brief, MNPs suspension (100 mg ml^{-1}) was vortexed for 30 s, then 10 µl MNPs (1 mg) was pipetted into a centrifuge tube containing 1 ml coating buffer (0.1 M sodium borate buffer, pH 9.5) and vortexed until homogeneously suspended. Afterwards the tube was placed on a magnet for 1 min and the supernatant was discarded. To perform the conjugation, 40 µl IL-4 capture antibody (250×) was added into the above tube, followed by 19.88 µl ammonium sulfate buffer (3 M in 0.1 M sodium borate buffer, pH 9.5). The tube was then incubated at 37 °C and shaken at 650 r.p.m. for 29 h. The tube was then placed on a magnet for 2 min and the supernatant was discarded; 59.88 µl blocking buffer (0.5 wt% BSA, 0.05 wt% Tween 20 in PBS buffer, pH 7.4) was added into the tube and then incubated and shaken at 650 r.p.m. for 21 h at 37 °C. After removing the supernatant, the conjugated MNPs were washed three times with the wash buffer (0.05 wt% tween 20 in PBS buffer, pH 7.4), and finally diluted to 1 mg ml^{-1} in wash buffer. During the process above, the MNPs were resuspended (30 s vortex) each time a new solution was added into the tube.

(2) ELISA of IL-4 protein
Standard IL-4 sample was diluted to 200, 100, 50, 25, 12.5 and 6.25 pg ml^{-1} using 1× ELISA diluent, to generate six samples for ELISA test. An eight-well fluidic device was created using the self-developed automatic machine. The device was blocked with 1× ELISA diluent for 1.5 h before use, then wash buffer was pumped into the device for 30 min (2 ml min^{-1}) to thoroughly wash the fluidic channels. A magnet was placed under the device (as shown in Supplementary Fig. 28) for the following MNPs-based ELISA.
The liquid device was first reconfigured to microreactor form, and the supernatant in the wells were removed with a pipette; 0.01 mg IL-4 capture antibody conjugated MNPs (10 µl solution) was mixed with 100 µl IL-4 solution, and then added into a well of the microreactor (in total: six test samples, one control sample (0 pg ml^{-1} IL-4) and one background sample (only TMB and stop solution)). After incubation for 2 h at room temperature, the device was reconfigured to its fluidic form and washed with wash buffer for 30 min (2 ml min^{-1}). In the same manner, 1× detection antibody (100 µl, 1 h incubation, 30 min wash), 1× HRP (100 µl, 30 min incubation, 30 min wash), 1× TMB (100 µl, 15 min incubation, 30 min wash) and stop solution (1 M phosphoric acid, 100 µl) were sequentially added into the device. The color and absorbance (450 nm) of the final solutions were recorded by a camera and microplate reader, respectively.

Characterizations

The contact angle was measured using a contact angle meter (JC2000D2, Zhongchen). The gas chromatography analyses were

performed on an Agilent 7890A gas chromatography system equipped with a flame ionization detector (HP-5 column). A Metrohm Autolab PGSTAT302N electrochemical workstation was employed to conduct all-liquid membrane-free battery performance tests. Ultraviolet–visible spectra were obtained from a UV-6100 double beam spectrophotometer (Shanghai MAPADA). The photographs were taken using a Sony A6300 equipped with a E30 F3.5 macro lens. The absorbance in molecular absorption tests and ELISA experiments were measured with a microplate reader (Synergy HT, BioTek).

Reporting summary

Further information on research design is available in the Nature Portfolio Reporting Summary linked to this article.

Data availability

The data that support the findings of this study are available in the main text and its Supplementary Information. Source Data are provided with this paper.

References

1. Austen Angell, C., Ansari, Y. & Zhao, Z. Ionic liquids: past, present and future. *Faraday Discuss.* **154**, 9–27 (2012).
2. Astoricchio, E., Alfano, C., Rajendran, L., Temussi, P. A. & Pastore, A. The wide world of coacervates: from the sea to neurodegeneration. *Trends Biochem. Sci* **45**, 706–717 (2020).
3. Gao, N. & Mann, S. Membranized coacervate microdroplets: from versatile protocell models to cytomimetic materials. *Acc. Chem. Res.* **56**, 297–307 (2023).
4. Abbas, M., Lipiński, W. P., Wang, J. & Spruijt, E. Peptide-based coacervates as biomimetic protocells. *Chem. Soc. Rev.* **50**, 3690–3705 (2021).
5. Liu, X. et al. Reconfigurable ferromagnetic liquid droplets. *Science* **365**, 264–267 (2019).
6. Daeneke, T. et al. Liquid metals: fundamentals and applications in chemistry. *Chem. Soc. Rev.* **47**, 4073–4111 (2018).
7. Wang, L., Lai, R., Zhang, L., Zeng, M. & Fu, L. Emerging liquid metal biomaterials: from design to application. *Adv. Mater.* **34**, 2201956 (2022).
8. Forth, J. et al. Building reconfigurable devices using complex liquid–fluid interfaces. *Adv. Mater.* **31**, 1806370 (2019).
9. Zarbin, A. J. G. Liquid–liquid interfaces: a unique and advantageous environment to prepare and process thin films of complex materials. *Mater. Horiz.* **8**, 1409–1432 (2021).
10. Piradashvili, K., Alexandrino, E. M., Wurm, F. R. & Landfester, K. Reactions and polymerizations at the liquid–liquid interface. *Chem. Rev.* **116**, 2141–2169 (2016).
11. Rao, C. N. R. & Kalyanikutty, K. P. The liquid–liquid interface as a medium to generate nanocrystalline films of inorganic materials. *Acc. Chem. Res.* **41**, 489–499 (2008).
12. Yang, H., Fu, L., Wei, L., Liang, J. & Binks, B. P. Compartmentalization of incompatible reagents within pickering emulsion droplets for one-pot cascade reactions. *J. Am. Chem. Soc.* **137**, 1362–1371 (2015).
13. Dudukovic, N. A. et al. Cellular fluidics. *Nature* **595**, 58–65 (2021).
14. Villar, G., Graham, A. D. & Bayley, H. A tissue-like printed material. *Science* **340**, 48–52 (2013).
15. Villar, G., Heron, A. J. & Bayley, H. Formation of droplet networks that function in aqueous environments. *Nat. Nanotech.* **6**, 803–808 (2011).
16. Montelongo, Y. et al. Electrotunable nanoplasmonic liquid mirror. *Nat. Mater.* **16**, 1127–1135 (2017).
17. Paratore, F., Bacheva, V., Bercovici, M. & Kaigala, G. V. Reconfigurable microfluidics. *Nat. Rev. Chem.* **6**, 70–80 (2021).
18. Yasuga, H. et al. Fluid interfacial energy drives the emergence of three-dimensional periodic structures in micropillar scaffolds. *Nat. Phys.* **17**, 794–800 (2021).
19. Xu, J., Xiu, S., Lian, Z., Yu, H. & Cao, J. Bioinspired materials for droplet manipulation: principles, methods and applications. *Droplet* **1**, 11–37 (2022).
20. Si, Y., Li, C., Hu, J., Zhang, C. & Dong, Z. Bioinspired superwetting open microfluidics: from concepts, phenomena to applications. *Adv. Funct. Mater.* **33**, 2301017 (2023).
21. Feng, S. et al. Three-dimensional capillary ratchet-induced liquid directional steering. *Science* **373**, 1344–1348 (2021).
22. Quéré, D. Wetting and roughness. *Annu. Rev. Mater. Res.* **38**, 71–99 (2008).
23. Vrancken, R. J. et al. Anisotropic wetting and de-wetting of drops on substrates patterned with polygonal posts. *Soft Matter* **9**, 674–683 (2013).
24. Ueda, E. & Levkin, P. A. Emerging applications of superhydrophilic–superhydrophobic micropatterns. *Adv. Mater.* **25**, 1234–1247 (2013).
25. Efremov, A. N., Grunze, M. & Levkin, P. A. Digital liquid patterning: a versatile method for maskless generation of liquid patterns and gradients. *Adv. Mater. Interfaces* **1**, 1300075 (2014).
26. Li, J., Ha, N. S., Liu, T. L., Van Dam, R. M. & Cj Kim, C.-J. Ionic-surfactant-mediated electro-dewetting for digital microfluidics. *Nature* **572**, 507–510 (2019).
27. Feng, W. et al. Harnessing liquid-in-liquid printing and micropatterned substrates to fabricate 3-dimensional all-liquid fluidic devices. *Nat. Commun.* **10**, 1802172 (2019).
28. Walsh, E. J. et al. Microfluidics with fluid walls. *Nat. Commun.* **8**, 816 (2017).
29. Dunne, P. et al. Liquid flow and control without solid walls. *Nature* **581**, 58–62 (2020).
30. Cai, L., Marthelot, J. & Brun, P.-T. An unbounded approach to microfluidics using the Rayleigh–Plateau instability of viscous threads directly drawn in a bath. *Proc. Natl Acad. Sci.* **116**, 22966–22971 (2019).
31. Jose, B. M. & Cubaud, T. Role of viscosity coefficients during spreading and coalescence of droplets in liquids. *Phys. Rev. Fluids* **2**, 111601 (2017).
32. Huang, Z. et al. A general patterning approach by manipulating the evolution of two-dimensional liquid foams. *Nat. Commun.* **8**, 14110 (2017).
33. Wong, T. S. et al. Bioinspired self-repairing slippery surfaces with pressure-stable omniphobicity. *Nature* **477**, 443–447 (2011).
34. Navalpotro, P., Palma, J., Anderson, M. & Marcilla, R. A membrane-free redox flow battery with two immiscible redox electrolytes. *Angew. Chem. Int. Ed.* **56**, 12460–12465 (2017).
35. Hirt, C. W. & Nichols, B. D. Volume of fluid (VOF) method for the dynamics of free boundaries. *J. Comput. Phys.* **39**, 201–225 (1981).
36. *ANSYS FLUENT 18.0 Theory Guide* (ANSYS, 2017).
37. Brackbill, J. U., Kothe, D. B. & Zemach, C. A continuum method for modeling surface tension. *J. Comput. Phys.* **100**, 335–354 (1992).

Acknowledgements

We thank C. Zhang for the help with the CFD simulations, and Z. Chen for an inspiring discussion on fluidic device applications. Z.G. thanks the support of National Key Research and Development Program of China (grant no. 2017YFA0700500) and National Natural Science Foundation of China (grant no. 52033002). X.D. is grateful for the support of the National Natural Science Foundation of China (grant nos. 22372032, 22002015) and the Natural Science Foundation of Jiangsu Province (grant no. BK20211560). Y.Z. is grateful for the support of the National Natural Science Foundation of China (grant no. 22202040), the Young Elite Scientists Sponsorship Program by CAST (grant no. 2022QNRC001), the China Postdoctoral Science Foundation

(grant nos. 2022M710688 and 2022TQ0064) and the Jiangsu Funding Program for Excellent Postdoctoral Talent (grant no. 2022ZB126).

Author contributions

X.D., Z.G., Y.Z. and S.L. conceptualized and designed this work. Y.Z., S.L., Z.C., Y.N., K.L., J. Zhou, Z.H., J. Zhang and S.D. performed the experiments. Y.Z., S.L., Z.C. and X.D. wrote the original paper. X.D. and Z.G. supervised the work. All authors analyzed the data and edited the paper.

Competing interests

Southeast University has filed patent applications on this work. The authors declare no other competing interests.

Additional information

Extended data is available for this paper at https://doi.org/10.1038/s44286-023-00023-z.

Supplementary information The online version contains supplementary material available at https://doi.org/10.1038/s44286-023-00023-z.

Correspondence and requests for materials should be addressed to Xin Du or Zhongze Gu.

Peer review information *Nature Chemical Engineering* thanks Thomas Cubaud, Govind Kaigala and Zuankai Wang for their contribution to the peer review of this work.

https://doi.org/10.1038/s44286-023-00023-z

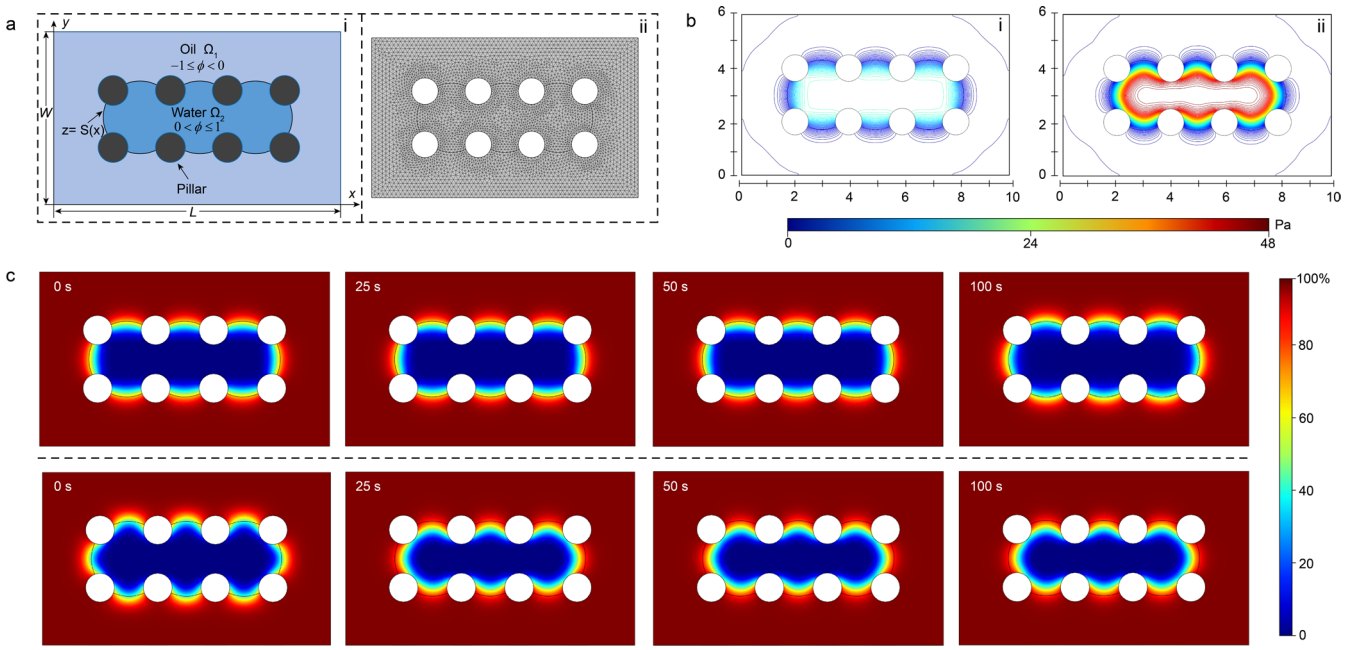

Extended Data Fig. 1 | Numerical simulation on 2D water layer in a pillared substrate. a, 2D physical model for simulation analysis. i: schematic demonstration, $L = 10$ mm, $W = 6$ mm. ii: meshing in the computational domain. **b**, The calculated pressure field (3 s after simulation starts) inside 2D water layer in the pillared substrates with $\theta = 100°$ (i) and $\theta = 150°$ (ii) respectively. In a highly hydrophobic pillared substrate, the oil-water interface exhibits much higher pressure and therefore a stronger tendency to contract. **c**, Images showing the simulated results of the changes in the volume fraction of oil phase within the computational domain in the pillared substrates with $\theta = 100°$ (top) and $\theta = 150°$ (bottom) respectively. In a highly hydrophobic pillared substrate, after simulation starts, the fraction of oil phase at the border of the water units significantly increases, compared with the limited changes in medium hydrophobic substrate. This indicates that the water units in highly hydrophobic pillared substrate have a strong tendency to contract. Notably, the simulation is performed on a 2D layer, thus the kinectics of the liquid behavior is distinct to the situation in 3D condition. More details see Methods.

https://doi.org/10.1038/s44286-023-00023-z

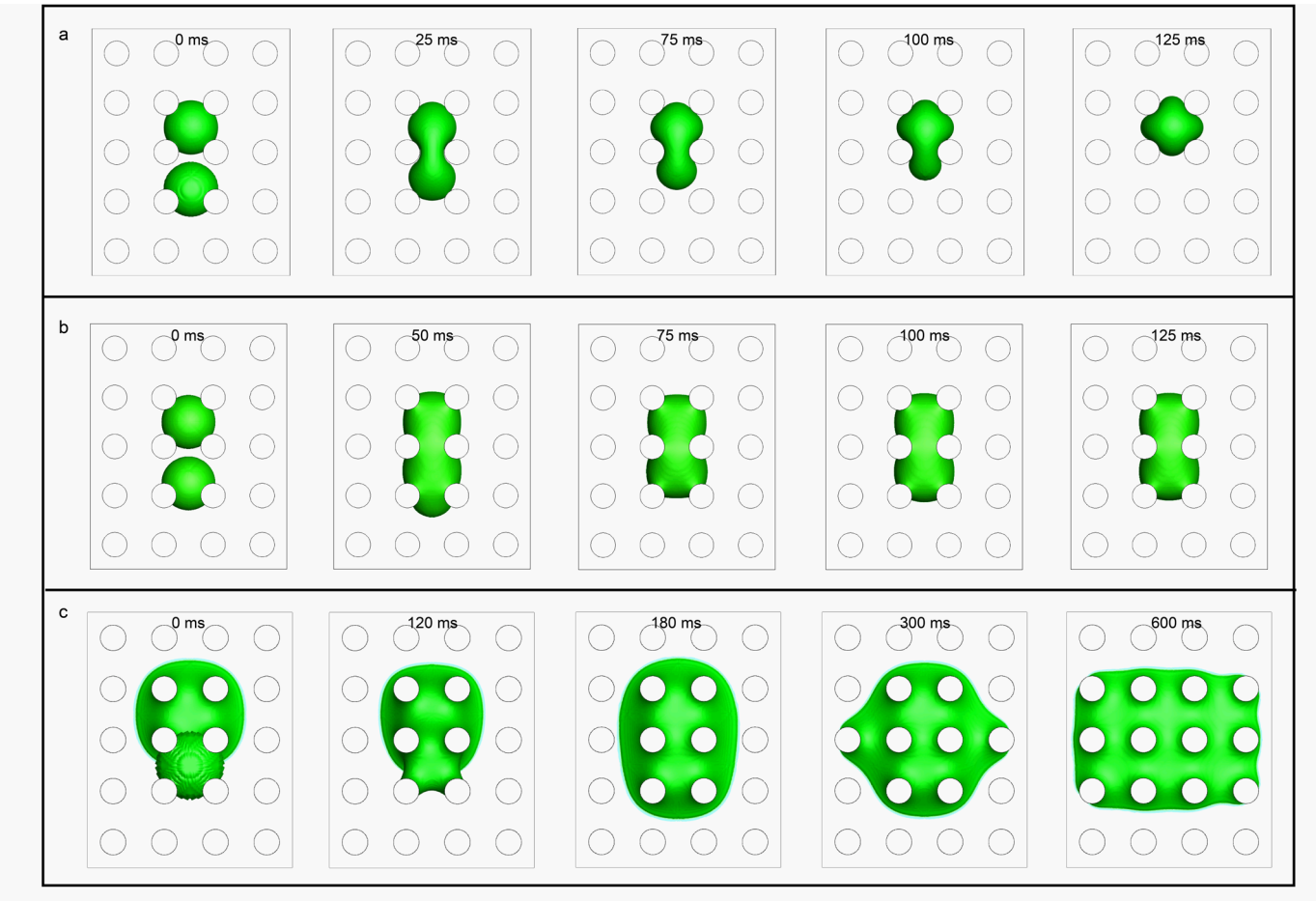

Extended Data Fig. 2 | CFD simulation on the combination of two water units in a pillared substrate. The WCAs of the substrate materials are (**a**) 170°, (**b**) 100° and (**c**) 30°. The droplets are added one by one, and the results are shown from top view (side view, 3D view and animations are shown in Supplementary Video 2). Notably, in the simulation, the pillared substrate was assumed to be perfect, with a homogeneous surface property and no structural defect, which is not exactly the same as observed experimental conditions (as shown in Fig. 1c). More details see Methods.

https://doi.org/10.1038/s44286-023-00023-z

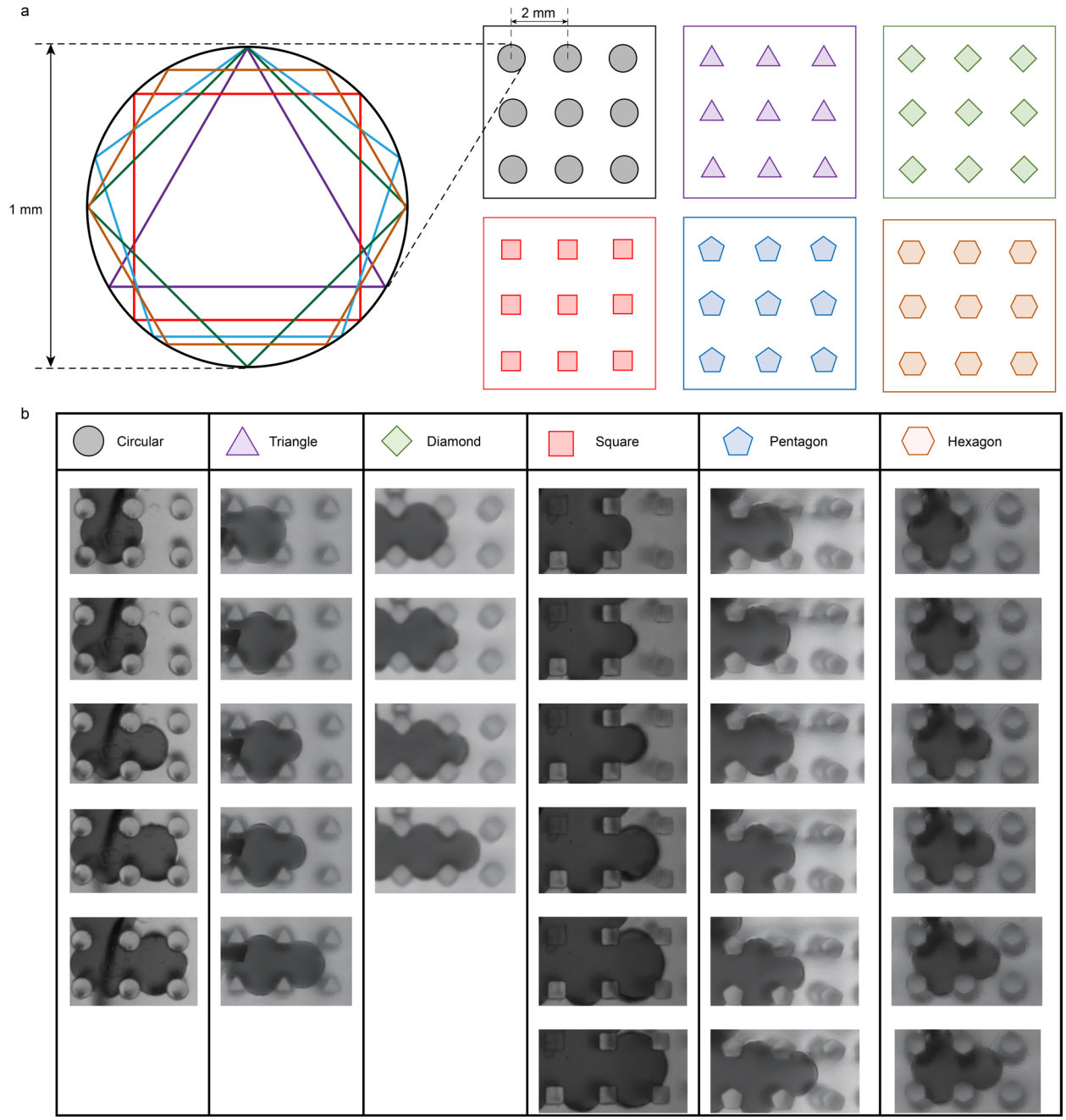

Extended Data Fig. 3 | Expansion of water–oil interface in pillar arrays with different geometries. a, Size and geometry of the pillars (height: 5 mm). **b**, Photos indicating the position of the water–oil interface in the pillar array during continuous water addition.

https://doi.org/10.1038/s44286-023-00023-z

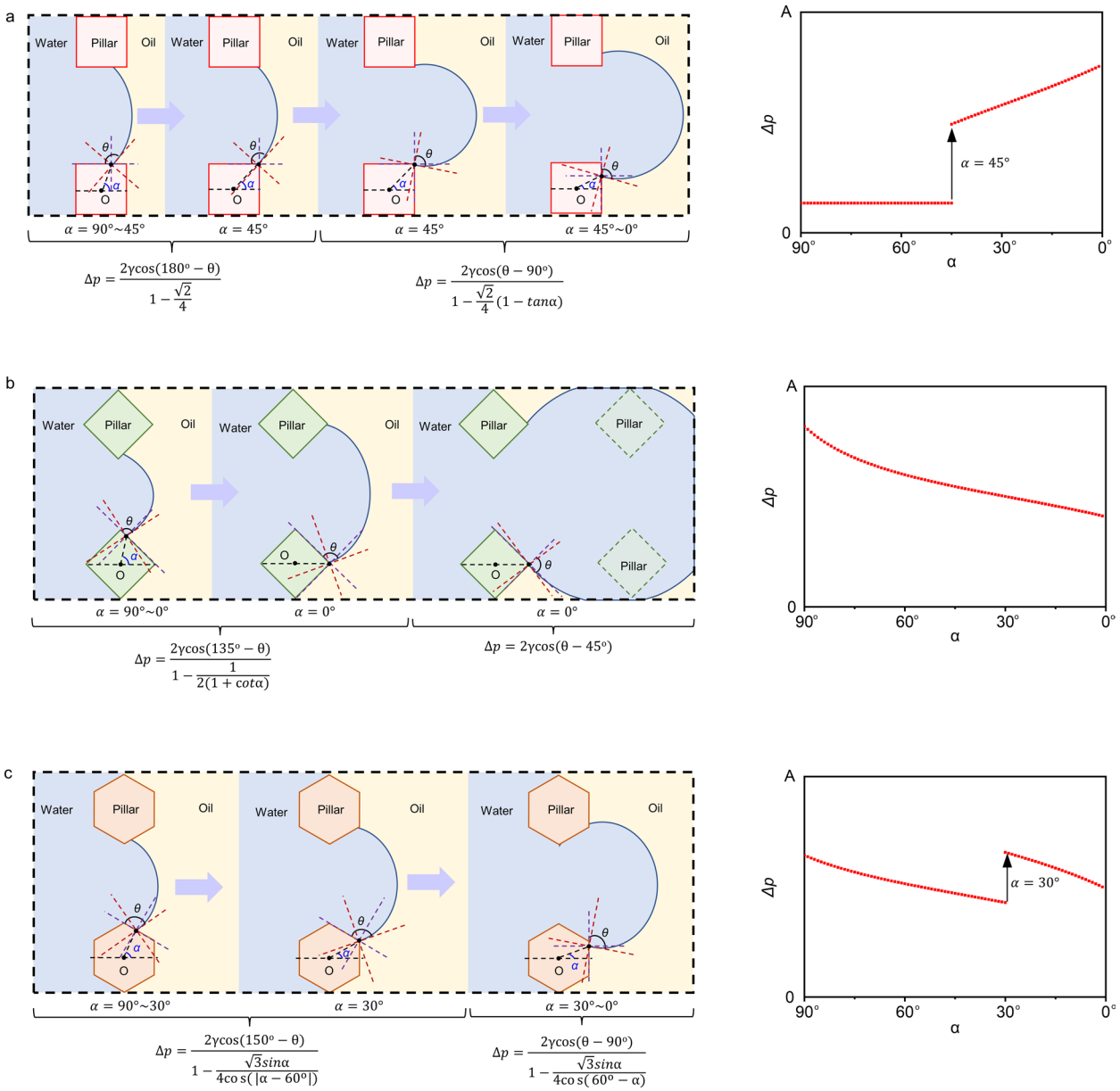

Extended Data Fig. 4 | Changes of LP of thin water layers during the expansion of water–oil interfaces in different pillar arrays. The left is the top view of the water layer at different stages, and the right is the calculated Δp value. **a**, Square pillar. **b**, Diamond pillar. **c**, Hexagon pillar. $A = \frac{4\gamma}{1mm}$. Δp: the Laplace pressure of the curved water–oil interface. γ: the surface tension of water. θ: the WCA of the substrate material. α: the angle indicating the position of the water–oil interface in the pillar array.

https://doi.org/10.1038/s44286-023-00023-z

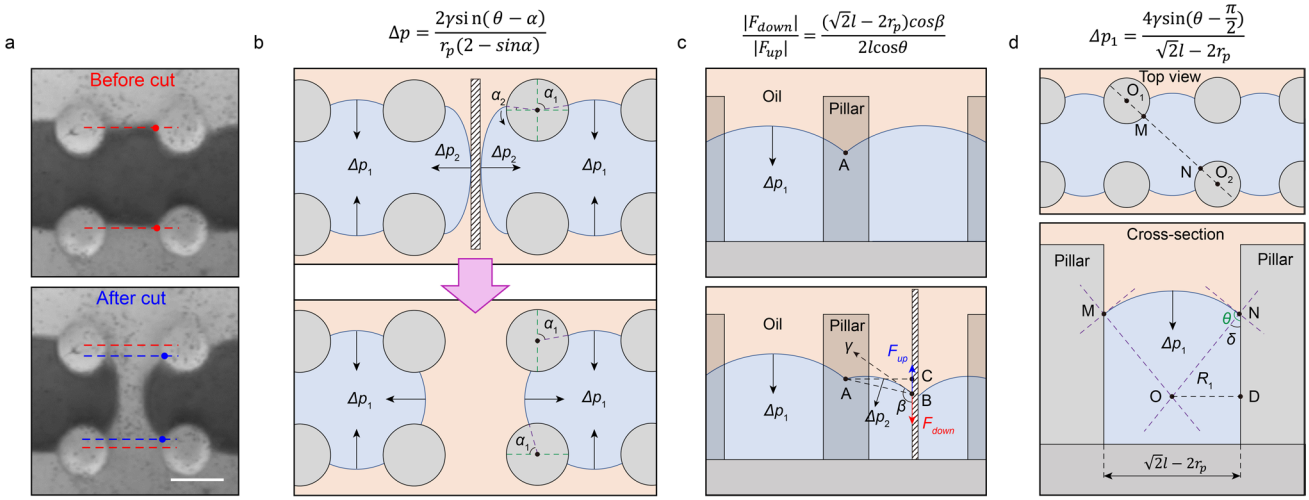

Extended Data Fig. 5 | The cutting process in water units. a, Photos of a water channel before and after being cut off with a fluorinated paper sheet. The red and blue points revealed the positions of tri-phase contact points from top view. Scale bars: 1 mm. **b-d**, A simplified model for the cutting process. **b**, The top view of a thin water layer when the water unit is completely cut off by a fluorinated paper sheet. **c**, The cross-sectional view of a thin water layer during the cutting process. **d**, A simplified model for the calculation of Δp_1 in (**c**). Δp: the Laplace pressure of the curved water–oil interface. γ: the surface tension of water. r_p: the radius of the pillar. l: the distance between pillar centers. θ: the WCA of the substrate material. α: the angle indicating the position of the water–oil interface in the pillar array. β: the WCA of the hydrophobic paper sheet. F_{up} and F_{down}: the upward and downward forces borne by the water–oil interface on the paper sheet, respectively. More details see Supplementary Note 3.

nature portfolio

Corresponding author(s): Xin Du, Zhongze Gu

Last updated by author(s): Dec 13, 2023

Reporting Summary

Nature Portfolio wishes to improve the reproducibility of the work that we publish. This form provides structure for consistency and transparency in reporting. For further information on Nature Portfolio policies, see our Editorial Policies and the Editorial Policy Checklist.

Statistics

For all statistical analyses, confirm that the following items are present in the figure legend, table legend, main text, or Methods section.

n/a	Confirmed
☐	☒ The exact sample size (*n*) for each experimental group/condition, given as a discrete number and unit of measurement
☐	☒ A statement on whether measurements were taken from distinct samples or whether the same sample was measured repeatedly
☐	☒ The statistical test(s) used AND whether they are one- or two-sided *Only common tests should be described solely by name; describe more complex techniques in the Methods section.*
☒	☐ A description of all covariates tested
☒	☐ A description of any assumptions or corrections, such as tests of normality and adjustment for multiple comparisons
☐	☒ A full description of the statistical parameters including central tendency (e.g. means) or other basic estimates (e.g. regression coefficient) AND variation (e.g. standard deviation) or associated estimates of uncertainty (e.g. confidence intervals)
☒	☐ For null hypothesis testing, the test statistic (e.g. *F*, *t*, *r*) with confidence intervals, effect sizes, degrees of freedom and *P* value noted *Give P values as exact values whenever suitable.*
☒	☐ For Bayesian analysis, information on the choice of priors and Markov chain Monte Carlo settings
☒	☐ For hierarchical and complex designs, identification of the appropriate level for tests and full reporting of outcomes
☒	☐ Estimates of effect sizes (e.g. Cohen's *d*, Pearson's *r*), indicating how they were calculated

Our web collection on statistics for biologists contains articles on many of the points above.

Software and code

Policy information about availability of computer code

Data collection	The contact angle was measured using a contact angle meter (JC2000D2, Zhongchen, China). The gas chromatography (GC) analyses were performed on an Agilent 7890A GC system equipped with a FID detector (HP-5 column). Metrohm Autolab PGSTAT302N electrochemical workstation was employed to conduct allliquid membrane free battery performance tests. UV-vis spectra were obtained from UV-6100 double beam spectrophotometer (Shanghai MAPADA Co. Ltd). The photos were taken using a Sony A6300 equipped with a E30 F3.5 macro lens. The absorbance in molecular absorption tests and ELISA experiments were measured with a microplate reader (Synergy™ HT, BioTek).
Data analysis	The software COMSOL Multiphysics 6.0 was employed to simulate 2D water layer in a pillared substrate and effect of density, surface tension on liquid, and gravity, formation in the pillared substrate. The software ANSY Fluent was adopted to simulate the 3D water droplets. PIVlab 2.62 in MATLAB version 9.14 (R2023a) was adopted to analyze the movement of tracer particles.

For manuscripts utilizing custom algorithms or software that are central to the research but not yet described in published literature, software must be made available to editors and reviewers. We strongly encourage code deposition in a community repository (e.g. GitHub). See the Nature Portfolio guidelines for submitting code & software for further information.

Data

Policy information about availability of data

All manuscripts must include a data availability statement. This statement should provide the following information, where applicable:

- Accession codes, unique identifiers, or web links for publicly available datasets
- A description of any restrictions on data availability
- For clinical datasets or third party data, please ensure that the statement adheres to our policy

The data that support the findings of this study are available in the main text and its Supplementary Information. Data presented in graphs were provided in Source Data file.

Research involving human participants, their data, or biological material

Policy information about studies with human participants or human data. See also policy information about sex, gender (identity/presentation), and sexual orientation and race, ethnicity and racism.

Reporting on sex and gender	N/A
Reporting on race, ethnicity, or other socially relevant groupings	N/A
Population characteristics	N/A
Recruitment	N/A
Ethics oversight	N/A

Note that full information on the approval of the study protocol must also be provided in the manuscript.

Field-specific reporting

Please select the one below that is the best fit for your research. If you are not sure, read the appropriate sections before making your selection.

☒ Life sciences ☐ Behavioural & social sciences ☐ Ecological, evolutionary & environmental sciences

For a reference copy of the document with all sections, see nature.com/documents/nr-reporting-summary-flat.pdf

Life sciences study design

All studies must disclose on these points even when the disclosure is negative.

Sample size	No sample-size calculation was performed. The sample size (n) for each experiment, was listed in corresponding figure legend.
Data exclusions	No data were excluded.
Replication	Experiments were repeated and experimental findings were reproducible.
Randomization	No living sample was adopted, and random allocation was not applicable in our research.
Blinding	Each experiment was conducted by a single researcher, who followed by multi-day protocols, so no blinding was applicable. Numerical simulation and data analysis were carried out by other researches, who were not aware of the experimental hypothesis at the time of performing the assays.

Reporting for specific materials, systems and methods

We require information from authors about some types of materials, experimental systems and methods used in many studies. Here, indicate whether each material, system or method listed is relevant to your study. If you are not sure if a list item applies to your research, read the appropriate section before selecting a response.

Materials & experimental systems

n/a	Involved in the study
☐	☒ Antibodies
☒	☐ Eukaryotic cell lines
☒	☐ Palaeontology and archaeology
☒	☐ Animals and other organisms
☒	☐ Clinical data
☒	☐ Dual use research of concern
☒	☐ Plants

Methods

n/a	Involved in the study
☒	☐ ChIP-seq
☒	☐ Flow cytometry
☒	☐ MRI-based neuroimaging

Antibodies

Antibodies used: human IL-4 uncoated ELISA kit (Invitrogen, catalog number 88-7046)

Validation: All antibodies were used according to the manufacturer's instructions. Validation of each antibody was done under standard information offered by the supplier.

Plants

Seed stocks: N/A

Novel plant genotypes: N/A

Authentication: N/A